



Evaluation of surface Lagrangian transport barriers in the Gulf of Trieste

F. Enrile^{a,*}, G. Besio^a, A. Stocchino^a, M.G. Magaldi^{b,c}, C. Mantovani^b, S. Cosoli^d, R. Gerin^d, P.M. Poulain^d

^a DICCA, Dipartimento di Ingegneria Civile, Chimica e Ambientale, Università degli Studi di Genova, Via Montallegro 1, 16145 Genova, Italy

^b ISMAR-CNR, S.S. di Lerici, Lerici, SP, Italy

^c Johns Hopkins University, Earth and Planetary Sciences, Baltimore, MD, USA

^d OGS, Istituto Nazionale di Oceanografia e Geofisica Sperimentale, Trieste, Italy



ARTICLE INFO

Keywords:

Lagrangian Coherent Structures (LCS)
Gulf of Trieste
CODE drifters
FTLE and FSLE
Single-particle tracking

ABSTRACT

The present work aims to detect Lagrangian transport barriers in the Gulf of Trieste by means of Lyapunov-exponent approach and tensorlines of the Cauchy-Green tensor. Lagrangian Coherent Structures (LCSs) are calculated employing 2D surface velocity fields measured by the coastal radars of the TOSCA EU research project (Tracking Oil Spills & Coastal Awareness Network). Moreover, surface drifters were deployed during the project. Comparisons between Eulerian velocity of HF-radar fields and Lagrangian velocity of drifters are carried out alongside single-particle tracking reliability. In particular, the possible influence of the data gaps in the HF-radar fields have been carefully considered. LCSs have proven to be robust against the quality of the starting HF-radar fields, leading to helpful insights in drifter positions. Indeed, after 24-hour integration the observed position of the drifter is approximately 1.5 km far from the nearest LCS, while a standard approach based on single-particle computations leads to larger errors (up to 5–7 km). However, such result must be properly interpreted taking into account the elongated nature of LCSs. A comparison between two common diagnostic tools of Lagrangian barriers is performed: Finite-Time and Finite-Size Lyapunov Exponent fields are compared in order to assess whether the patterns detected by the two measures are comparable. Finally, a joint analysis between LCSs and single-particle tracking is carried out and the results suggest that it would be desirable to couple these two approaches in real applications.

1. Introduction

Knowledge of the fate of pollutants and biological quantities in coastal environments is of paramount importance owing to their impact on natural ecosystems. Several approaches have been proposed in order to tackle this challenging task. However, the most promising strategies shall be based on a Lagrangian point of view, being a natural framework for analyzing mixing processes. Among the available Lagrangian models and measures, Lagrangian Coherent Structures, hereinafter LCSs, are known to strongly control and govern the transport of mass in disparate complex fluid flows (Boffetta et al., 2001; Shadden et al., 2005). In fact, LCSs act as material lines/surfaces within a given flow field and, thus, mass transport is, in principle, inhibited through them and a possible spatial/temporal segregation of pollutants and nutrients might be generated and sustained for a given circulation pattern.

Their heuristic identification mainly relies on the application of Lyapunov-exponent-based diagnostic tools. In particular, heuristic LCSs are defined as the ridges, locus of maxima, in both Finite-Time and

Finite-Size Lyapunov Exponent (FTLE and FSLE, respectively) scalar fields (Shadden et al., 2005). However, several restrictive conditions (Haller, 2011; Karrasch and Haller, 2013; Allhouse and Peacock, 2015b) are needed to actually detect transport barriers. Despite these restrictions, the application of FTLEs and FSLEs continues to soar, especially in geophysical applications. The success of this approach can be found in its relatively simple implementation and great efficacy in highlighting transport barrier candidates and detecting the directions along which transport is likely to develop (Lekien et al., 2005; Peng and Dabiri, 2009; Shadden et al., 2009; Huhn et al., 2012; Cencini and Vulpiani, 2013; Berta et al., 2014b; Hernández-Carrasco et al., 2014; St-Onge-Drouin et al., 2014; Allhouse and Peacock, 2015a; Garaboa-Paz et al., 2015). However, only a few examples of the simultaneous implementation of both temporal and spatial analysis can be found in the literature, often providing contrasting indications. Boffetta et al. (2001) show that FTLEs are limited to small-scale properties of dispersion, whereas FSLEs are the most efficient method for detecting large-scale cross-stream barriers. On the contrary, FTLEs have been shown to better

* Corresponding author.

E-mail address: francesco.enrile@hotmail.it (F. Enrile).

capture recirculation regions than FSLEs (Sadlo and Peikert, 2007). In a recent paper, Peikert et al. (2014) show that, if properly calibrated by similarity measures, both FTLEs and FSLEs may produce comparable results that can be interchangeably used for most purposes in flow visualizations. Further investigation, especially in the context of realistic geophysical flows, will thus provide valuable information on the mutual importance of the Lagrangian measures, namely FTLE and FSLE. Indeed, oceanic coastal circulations, as the ones considered in the present study, may represent a challenging task along this direction. In fact, the computation of the FTLEs and FSLEs fields requires an in-depth knowledge of the circulations velocity field.

This requirement is only partially fulfilled when either satellite altimeter data (Harrison and Glatzmaier, 2012), numerical models (Haza et al., 2007, 2008) or coastal observations (Haza et al., 2010; Berta et al., 2014b) are employed. As a matter of fact, temporal and spatial resolution of the latter datasets may not be adequate to resolve the range of scales typical of the high Reynolds number of oceanic or coastal circulations. In this case, observations in coastal areas have recently benefited by the use of high-frequency (HF) radars, the number of which is rapidly increasing owing to their better resolution with respect to other oceanographic observational systems and reliability of the measured velocities. HF-radars provide maps of surface velocity with ranges up to 100 km, horizontal resolution of the order 1.5–3 km, and temporal resolution of the order of 0.25–1 h (Gurgel et al., 1999; Harlan et al., 2010; Paduan and Washburn, 2013). HF-radar velocity measurements have been validated against Lagrangian drifter observations leading to averaged differences mostly within the range 3–5 cm/s, whereas larger deviations, e.g. around 20 cm/s, can be attributed to the unresolved spatial variability of velocity fields at subgrid scale (Ohlmann et al., 2007). Although the accuracy reached with HF-radars is more than satisfactory, still several issues exist regarding the radar coverage and its operability in particular conditions. In fact, the measurable coastal areas strongly depends on the coastline geometry and on the presence of fixed and/or temporary obstacles of different nature. Furthermore, insufficient signal-to-noise ratios can be registered within some radar cells owing to severe weather conditions (strong winds, rough seas with large waves) or external interference at the radar emission frequency. As a result, holes and gaps can appear in the HF radar velocity maps and the reliability of the transport estimates based on these measures can be questionable. This can be particularly true in small scale embayments or coastal gulfs where radar resolution plays a critical role as well as local processes.

So far, only a few applications of HF-radar datasets have been used for FSLE calculations in the Mediterranean Sea (Haza et al., 2010; Berta

et al., 2014b), compared to the numerous applications in the Atlantic and Pacific oceans. Indeed, a direct comparison of FSLE ridges with drifter data in the Mediterranean Sea has been discussed only in Haza et al. (2010).

The present study tries to cover this gap of knowledge, at least in part, and aims to either address some methodological issues and provide quantitative estimations of the relevant Lagrangian parameters.

Regarding the LCS detection and application we aim to detect both heuristic LCSs, through FTLEs, FSLEs and LCSs, applying the geodesic theory of transport barriers (Haller and Beron-Vera, 2012). Besides, we intend to assess whether, starting from the same high Reynolds number turbulent fields, FTLE and FSLE techniques lead to similar heuristic LCSs and how accurately the latter compare with drifter observations in a Mediterranean small scale area. Moreover, we aim to test the robustness of these Lagrangian analysis when applied to HF-radar fields. In fact, quite often the HF-radar velocity fields show several spatial gaps, mostly owing to signal problems, and we intend to show that FTLE-FSLE-LCS based methods are less sensitive to these data gaps with respect to standard Lagrangian approaches, e.g. absolute dispersion. The importance of this aspect could easily be appreciated having in mind the possible application of risk monitoring and Search and Rescue (SaR) operations based on HF-radar information.

In this study, we focus on a small ($\sim 20 \text{ km} \times 20 \text{ km}$) Mediterranean gulf, namely the Gulf of Trieste, GoT in the following, located in the Northeastern Adriatic Sea. The GoT area was targeted by the EU-MED project TOSCA (Tracking Oil Spills and Coastal Awareness network, <http://www.tosca-med.eu>) to investigate and test science-based methodologies, best practices, and response plans in case of accidents at sea (Bellomo et al., 2015). A coastal monitoring network based on HF-radars has been established under the framework of TOSCA with a special emphasis on oil spill pollution and on SaR operations. Thus, the results of the present work have practical applications and can be useful to indicate how reliable Lagrangian transport estimates based on HF-radars velocity fields in case of accidents at sea are.

The paper is organized as follows: in Section 2 a description of the HF-radar network and drifters used during the TOSCA project is provided. Section 3 is dedicated to the definition of FSLEs and FTLEs and their comparison. Section 4 assesses the influence of HF-radar data gaps on the Eulerian and Lagrangian properties of the surface circulation. Section 5 is dedicated to the comparison of drifter trajectories and heuristic LCSs while Section 6 takes into account rigorous LCSs. Finally, the conclusions are drawn in Section 7.

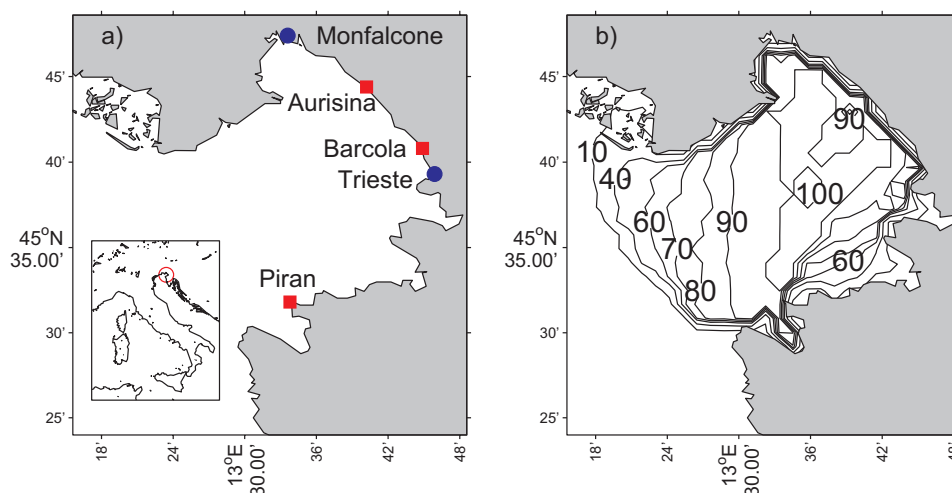


Fig. 1. Radar network locations in the Gulf of Trieste, red squares of Panel a), and percent coverage of the velocity field data derived from HF-radar measurements for April 23 to April 30, 2012, Panel b). (For interpretation of the references to color in this figure legend, the reader is referred to the web version of this article.).

2. Datasets of the Trieste Gulf area

The GoT is a shallow semi-enclosed basin in the NE Adriatic Sea (see Fig. 1) with a maximum depth of 25 m. Circulation is generally cyclonic, forced by the incoming Istria coastal current at the southern border, but intense and frequent wind conditions from the northeastern quadrant produce an east to west current at the surface layer (Malačić and Petelin, 2009). Its oceanographic properties are variable due to pronounced seasonal cycles resulting in thermal stratification during summer and to the formation of strong salinity gradients originated by the contrasting effects of fresh water runoffs and seawater exchange at the open boundary (Malačić and Petelin, 2001).

2.1. High-frequency radar

HF-radar operation principle is based on the “Bragg scattering” of electromagnetic waves over a rough sea (Crombie, 1955). Radar signals scattered off ocean waves that are exactly half of the transmitted signal wavelength, add coherently and result in a strong return of energy at a very precise wavelength. The Doppler-frequency shift of this return provides information about the velocity of the scattering ocean waves, telling apart speed contributions due to both ocean currents and wave motions (Gurgel et al., 1999).

A network of HF-radars has been installed in the GoT area as part of the TOSCA project in order to provide a full coverage of the gulf area and its closest surroundings. The network consists of three monostatic CODAR SeaSonde systems (Fig. 1), namely installed at: Aurisina (3°40′ 8.5″ E; 45°44′ 28.9″ N; Italy), Piran (13°33′ 45.8″ E; 45°31′ 42.8″ N; Slovenia) and Barcola (13°45′ 15.0″ E; 45°40′ 43.0″ N; Italy). The working frequency for all three systems has been set to 25 MHz, bandwidth to 150 kHz, for a radial resolution of 1 km. The network configuration ensures an operating range up to 30 km, with an angular resolution of 5° and employs the MUSIC (Multiple Signal Classification) direction finding algorithm (Schmidt, 1986) to derive radial currents on a hourly basis. The standard proprietary SeaSonde Software (Radial Suite and Combine Suite 10R5) is used to geometrically combine the radial information from the HF radar systems and produce total vectorial maps of surface current on a 1.5 km × 1.5 km Cartesian grid. The SeaSonde Software uses a least-square fitting method (Lipa and Barrick, 1983; Barrick and Lipa, 1986) to interpolate radials within a local circle with a radius of 2 km. The SeaSonde Software also performs standard quality control checks on both radial and total vectors, removing spikes and grid points with large geometrical dilution of precision (GDOP), i.e. points where radial velocities within the local circle are too close to parallel (stability angles lower than 15° and larger than 165°).

In this work we will consider the surface current information measured by the HF radar network during the period of the TOSCA 2012 experiment, i.e. during April 23–30, 2012. During this period, data gaps have been partially filled through a linear interpolation both in space and in time, trying to avoid more complex operations available in literature, like for example the DINEOF analysis (Alvera-Azcárate et al., 2009, 2011). The motivation for this choice is twofold. On one hand, we intend to mimic the operational procedures employed in case of maritime accidents causing spills, when timing is critical and fast computation is a priority, in lieu of employing more accurate and time consuming techniques. On the other hand, we aim to test the robustness of the Lagrangian analysis even in case of data gaps or with simple and quick filling procedures.

2.2. CODE drifters

During the 2012 TOSCA April experiment in the GoT, a total number of 41 CODE (Coastal Ocean Dynamics Experiment) drifters (Davis, 1985; Poulain, 1999) have been launched. This number includes the cases where drifters were caught and re-launched in order to maintain coverage of the HF radar area. CODE drifters consist of a 1-m

vertical structure with four vertical sails that extend radially. The entire structure is immersed in the first meter of water, therefore they are suited for a direct comparison with the HF radar velocities. They are designed to minimize slippage due to the direct action of wind and waves, whose errors are estimated to be within 1–3 cm/s for wind up to 10 m/s (Poulain et al., 2009). CODE positions are retrieved every 15–60 min via Global Positioning System (GPS) receivers with an accuracy of approximately 5–10 m. Drifter raw data have been edited to remove outliers and spikes and interpolated at uniform 1-h intervals (Hansen and Poulain, 1996). Drifter velocities have been computed by central finite differences.

It is important to note that HF-radar and drifter-based velocities may differ because of the nature of their sampling, both in the vertical and horizontal dimensions. In the vertical, HF-radar velocities are the exponentially-weighted averages of the upper ocean velocity profile. As a result, they depend on the vertical shear of the horizontal current and on the HF-radar frequency (Stewart and Joy, 1974; Ivonin et al., 2004). For the working radar frequency of 25 MHz used in GoT and under the assumption of a linear vertical shear, the radar measurement corresponds to an average over an effective depth of about 50 cm which is half the vertical dimension of the CODE structure. The mismatch between the two types of measurements is even more evident in the horizontal dimension: HF radar velocities are quantities averaged over grid cells whose sizes are in order of kilometers. Drifters, on the contrary, are affected by scales of motions comparable to their physical horizontal size, i.e. of the order of 1 m for the CODE-type. In this study, we consider 26 of the above CODE drifter trajectories, discarding those lasting less than 12 h. Bellomo et al. (2015) carried out a detailed validation of the HF-radar velocity data against the direct measurements of the Lagrangian velocity using the CODE drifters. In particular, the radial velocities coming from the elaboration of the HF-radar signals showed a root-mean square (rms) difference of about 10 cm/s, which is in the range of 5–15 cm/s commonly accepted for similar measures (Paduan and Rosenfeld, 1996; Chapman et al., 1997; Ohlmann et al., 2007; Molcard et al., 2009; Huhn et al., 2012) and comparable with previous observations in the surroundings of the GoT described in Cosoli et al. (2013), where averaged rms velocity differences in a range from 7.5 cm/s to 9.9 cm/s are reported.

3. Detection of heuristic LCSs by means of Lyapunov exponents: FSLEs and FTLEs

The starting point of the Lagrangian analysis presented in the remaining part of the work is

$$\dot{\mathbf{x}} = \mathbf{v}(\mathbf{x}, t) \quad (1)$$

which represents the trajectory of a particle seeded on the domain. Eq. (1) consists in a non-autonomous dynamical system and in this framework LCSs are widely used to characterize horizontal dynamics. Hyperbolic LCSs are distinguished material lines that exert locally the strongest attraction and repulsion on nearby trajectories. Being material lines LCSs behave as transport barriers, not being crossed by tracers. Note, however, that ridges in FTLE and FSLE fields do not always correspond to actual material lines. This is the reason why in the following we will introduce a different approach in the LCSs detection, based on the geodesic theory. We still retain helpful the evaluation of the FTLE and FSLE fields in order to provide a spatial description of the most dynamically active flow regions.

The detection of heuristic LCSs by FTLEs is pursued according to Shadden et al. (2005). In this context FTLEs can be considered a finite-time average of the maximum expansion rate that a pair of particles advected by the flow can experience in a finite-time interval T . The definition of the FTLE is

$$\sigma_0^{t_0+T}(\mathbf{x}) = \frac{1}{|T|} \log \sqrt{\lambda_{\max}} \quad (2)$$

where λ_{max} is the maximum eigenvalue of the Cauchy-Green tensor, t_0 is the initial time and T is the integration time, i.e. the finite-time interval over which the FTLE is calculated. Defining the deformation gradient as

$$F = \frac{d\mathbf{x}(t_0 + T)}{d\mathbf{x}(t_0)} \quad (3)$$

the Cauchy-Green Tensor is evaluated as:

$$C_G = F^T F. \quad (4)$$

The Cauchy-Green tensor is a linear operator represented by a symmetric and positive definite matrix that expresses a rotation-independent measure of deformation, since a pure rotation does not produce any strain (Truesdell and Noll, 2004). FTLEs form a scalar field and heuristic LCSs are located by the ridges of these scalar-field maps obtained from the above operator (Shadden et al., 2005). Analogously to FTLEs, FSLEs provide a measure of the dispersion as a function of the spatial resolution (Boffetta et al., 2001). The aim is to evaluate the time needed for a pair of particles to reach a defined final separation δ_f . The definition of FSLE reads as:

$$\Lambda(\mathbf{x}, \delta_0, \delta_f) = \frac{1}{|\tau|} \log\left(\frac{\delta_f}{\delta_0}\right) \quad (5)$$

where δ_0 is the initial separation between the pairs of particles and δ_f is the target final separation between the same pair of particles reached after a generic time interval τ .

Results achieved by FSLEs and FTLEs are conceptually different, even if their common aim is the search for a rate of a separation. FSLEs operate at fixed length scales: the ratio $\alpha = \delta_f/\delta_0$ is fixed whereas τ , which is the time needed to reach the final separation, is free to vary. On the contrary, FTLEs operate with a fixed time-scale T and detect a separation rate that changes from point to point.

Heuristic LCSs can be divided into two broad classes: repelling, in forward time, and attracting, in backward time. Eq. (1) can be solved in forward time, i.e. from the initial time t_0 to the end of the time interval, to locate repelling structures and in reverse time, i.e. from the end of the time interval to the initial time t_0 , to detect attracting structures (Shadden et al., 2005; Hernández-Carrasco et al., 2011; Huhn et al., 2012; Allshouse and Peacock, 2015a). These structures can be viewed as finite-time stable and unstable manifolds locating, respectively, regions of expansion and contraction of fluid particles.

3.1. Parameters choice for FTLE and FSLE fields detection

A key parameter in order to highlight heuristic LCSs in FTLE fields is the integration time T . In analogous coastal application, Shadden et al., (2005, 2009) and Huhn et al. (2012) used integration times with an order of magnitude of hours. In the present study, we perform a sensitivity analysis depending on the integration time, which has been changed in a range between five and fifty hours.

Fig. 2 shows different FTLE fields evaluated at the increase of the integration time T . As T increases the ridges, i.e. the Lagrangian structures, clearly emerge. Integration times tending to either zero or infinity lead to, respectively, fields dominated by local strain without fully developed barriers on the domain (Panel a) of Fig. 2 or uniform fields (Panel d) of Fig. 2. This behavior has been investigated by Abraham and Bowen (2002) computing the mean value of the Lyapunov coefficient and their standard deviation depending on the integration time. These statistics tend to decrease as the integration time increases. Based on this observation, we decide to adopt a value of 25 h, high enough to let Lagrangian structures appear clearly and showing the highest correlation with analogous FSLE fields, as described in the next Section. In addition, since in Section 5 we will perform simulations of drifters with a 24 h reseeding, such a choice of the integration time enables us to look for FTLE fields whose information is evaluated on the same time scale of the reseeding process.

In analogy to the computations of FTLE fields, it is possible to evaluate different FSLE fields varying the initial separation δ_0 and the target final separation δ_f . Haza et al. (2008) suggested that the minimum ratio between final and initial separation $\alpha = \delta_f/\delta_0$ must be chosen so that the time required for particle pairs to separate from δ_0 to δ_f is longer than the time resolution Δt of the velocity dataset, equal to 1 h in the present case study. In order to ensure such a condition a value of $\alpha = 7$, as already used by Haza et al. (2008), is adopted. Fig. 3 shows FSLE fields at the varying of the ratio α .

3.2. FTLE and FSLE comparisons

Following Peikert et al. (2014), we compare FTLE and FSLE maps by calculating their correlation coefficient. FTLE and FSLE fields adopted for the analysis are obtained by seeding of an initial grid with a regular spacing of 200 m. The resulting FSLE fields might present some gaps, where the computed separation does not reach the target separation δ_f . Hence, the correlation coefficient evaluation is carried out taking into account only the corresponding values of FTLE fields to actual values of FSLE fields, while FTLE regions where FSLEs are not defined are disregarded by this analysis.

The correlation coefficient is defined as

$$\text{corr}(f, g) = \frac{\text{cov}(f, g)}{\sqrt{\text{var}(f)\text{var}(g)}} \quad (6)$$

where f and g are the FSLE/FTLE fields and its results are reported in Table 1 as a function of integration time T and final separation δ_f .

The present results shows that the correlation coefficient reaches values higher than 0.8 for integration time greater or equal to about a day, i.e. 25 h, regardless the final separation. Moreover, the combination of $T = 25$ h and $\delta_f = 1400$ m presents the highest value, i.e. around 0.88. This integration time is approximately twice the Lagrangian integral time, i.e. the average between the integrals of normalized velocity autocorrelations in the x and y directions (LaCasce, 2008; Fischer et al., 1979). In the present case, the Lagrangian integral time scale is approximately 12 h and justifies the fact that adopting T smaller than this time scale does not provide any significant heuristic LCSs (cf. Panel a) of Fig. 2.

4. Influence of HF-radar data gaps on the Eulerian and Lagrangian properties of the surface circulation

In this section we intend to estimate the role of data gaps in the HF-radar velocity measurements on the estimation of Eulerian and Lagrangian quantities, with a particular attention to the prediction of numerical trajectories. It is not unlikely that HF-radar velocity fields might experience the presence of data gaps for a particular time frame, for the reasons already discussed. An example is shown in Fig. 4, where quite a significant part of the GoT basin is not covered by the velocity data. In this case, interpolation/extrapolation algorithms are implemented in order to overcome this problem. The question now being asked is what influence might have velocity gaps on the estimation of different Eulerian and Lagrangian properties of the surface circulation.

Herein, we follow a similar approach as the one adopted by Bellomo et al. (2015), with the only difference that the present analysis has been carried out using the total Eulerian velocity fields instead of the radial velocities, as in Ohlmann et al. (2007) where a specific analysis using the Eulerian velocities has been discussed. All Authors provided a measure of agreement between HF-radar velocities and drifters velocities in term of time-averaged root mean square of the differences. We define the differential root mean square U_{rms} as

$$U_{rms} = \sqrt{(u_{Euli} - u_{Lagi})^2 + (v_{Euli} - v_{Lagi})^2} \quad (7)$$

where the overbars stand for averages over the drifter positions, u_{Lagi} and v_{Lagi} are the drifter velocity components at the i -th position and u_{Euli}

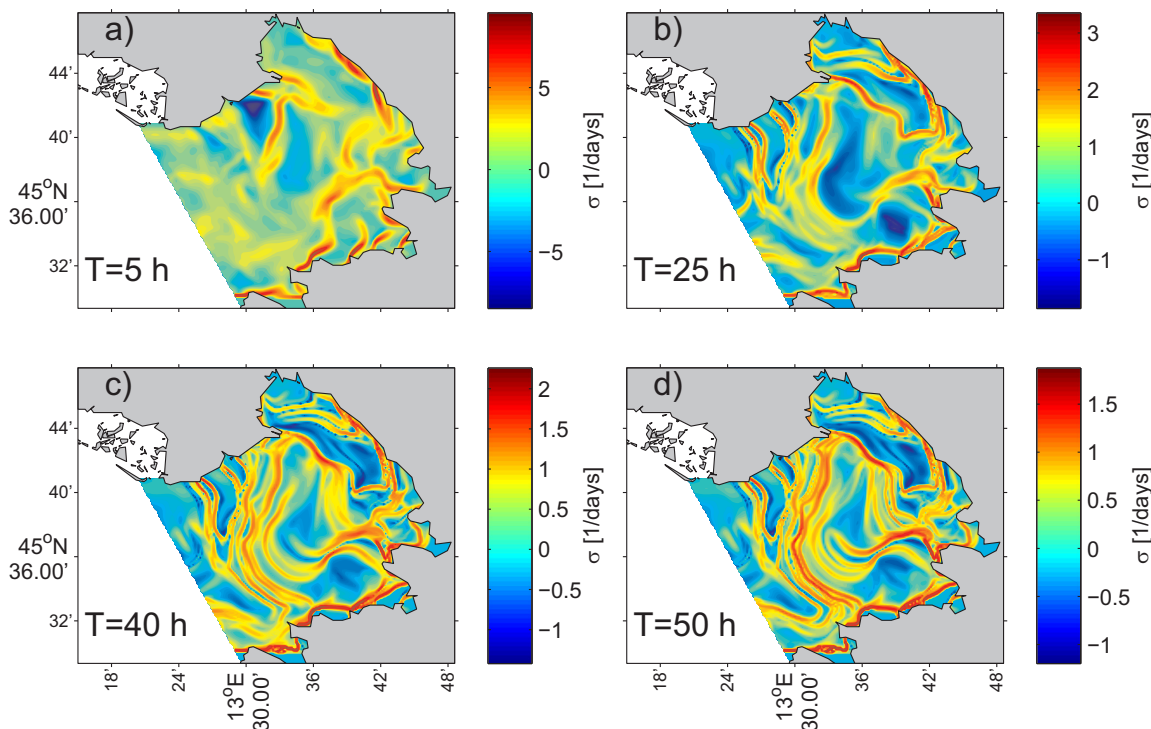


Fig. 2. FTLE fields calculated increasing the integration time T .

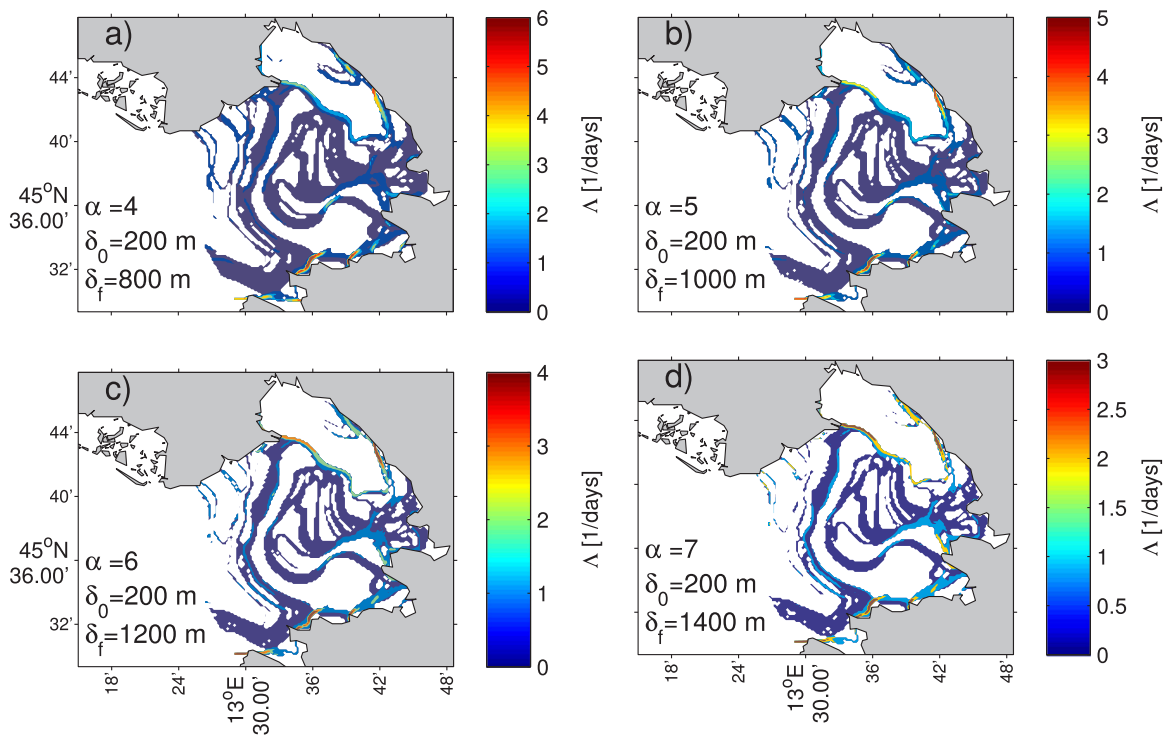


Fig. 3. FSLE fields calculated with $\delta_0 = 200$ m and $\delta_f = 800, 1000, 1200$ and 1400 m.

and v_{Eul_i} are the HF-radar velocity components interpolated on the same position. The computation of U_{rms} has been repeated for three cases: using the complete dataset, including the data gaps, excluding the data gaps from the data and, finally, considering only the data gaps. The comparison among the three cases will help in highlighting the influence of the data gaps in the HF-radar measurements.

The resulting values of the U_{rms} for the three cases are shown in Fig. 5 for each drifter (colored dots) and the corresponding weighted

average value (colored lines). Starting from the case where the whole data are considered, red dots and line, the results suggest that the data gaps generally tend to decrease the accuracy of the velocity estimation, leading to higher U_{rms} (blue dots and line). On the other hand, excluding the data gaps leads to lower U_{rms} (black dots and line). With respect to the general trend described above, there are some exceptions. In fact, quite a few drifters do not encounter any HF-radar data gaps, e.g. drifters 6, 20 and 24. Moreover, the expected improvement derived

Table 1

Correlation coefficient between FTLE and FSLE fields calculated for different values of the integration time T and of the final separation δ_f . The highest correlation is highlighted.

δ_f	800 m $\alpha = 4$	1000 m $\alpha = 5$	1200 m $\alpha = 6$	1400 m $\alpha = 7$
5 h	0.6596	0.7813	0.7742	0.7657
25 h	0.8240	0.8695	0.8776	0.8790
40 h	0.8074	0.8450	0.8570	0.8645
50 h	0.8047	0.8368	0.8511	0.8608

from excluding the data gaps does not occur in several cases, see Drifter 5, 7, 9, 22 and 51, or it is not detectable, e.g. Drifter 17 and 47.

However, the estimated value of U_{rms} considering only the data gaps remains well contained within the interval of one standard deviation with respect to the average value computed with the whole data, suggesting that, from an Eulerian point of view, they do not influence considerably the quality of the total velocity fields. Note that the estimated values are consistent with the analysis performed by Bellomo et al. (2015) with the radial velocities and are in line with the usual expectations of difference of the order of 5–15 cm/s. These results are in agreement with Rohrs et al. (2015) where it is shown that HF radars do not measure Stokes drift but mainly the Eulerian current.

It is now interesting to analyze the difference that can arise numerically simulating Lagrangian trajectories that should represent the real path of the deployed drifters. The synthetic trajectories have been computed following the same approach described in Bellomo et al. (2015), i.e. the numerical simulations have been initialized at the same time and position with respect to the deployed drifters and a reseeding procedure is applied at constant time intervals. Every 24 h a new numerical trajectory is restarted using as initial conditions the position of the observed drifters. Such a procedure is commonly adopted in numerical simulations of drifters (Berta et al., 2014a). Example of the comparison between observations and numerical prediction with or without a reseeding procedure are shown in Fig. 6 for three cases, namely Drifter 6, 29 and 42. Among the available data sets, we have chosen these three examples as typical cases where the path of the deployed drifters encounters HF-radar velocity fields with no gaps (Drifter 6), quite a few gaps (Drifter 29) and several gaps (Drifter 42). In all cases, the numerical trajectories often tend to move away from the observed paths. This behavior could be ascribed to two concurrent effects. On one hand, data gaps in the vectorial velocity field derived from HF-radar measurements plays a negative role on the quality of dispersion computations, as for the case of Drifter 42 and, partially, for Drifter

29. In fact, the simulated trajectory of Drifter 42 clearly diverges from the observed one especially in the central part of the GoT. For this case several data gaps are observed, as reported in Fig. 7 with shaded regions. On the other hand, the differences detected for Drifter 6, where no gaps are registered, should be caused by the coarseness of the HF-radar velocity fields that does not allow for a detailed description of small scale dynamics. Besides, radar velocities do present uncertainties due to, for example, errors in the direction-finding algorithm. However, this effect occurs for all Drifters and, then, the lower accurate comparison in cases as Drifter 42 is necessary related to the data gaps. Indeed, separations greater than 6 km are reached over 24 h. In the next section we will deepen the consequence of the discussed aspects and show how a description based on LCSs might overcome, at least in part, the flaws of the particle-simulation approach.

5. Heuristic LCSs detection vs drifter observations

Robustness of Lagrangian structures detected by Lyapunov-exponent diagnostic tools to velocity errors and scaling is well-known (Haller, 2002; Hernández-Carrasco et al., 2011). Such a property allows the joint analysis of Lagrangian structures and drifter trajectories despite the coarseness of velocity fields and the presence of missing data. Shadden et al. (2009) and Huhn et al. (2012) already showed that drifter trajectories are tied to Lagrangian structures. Furthermore, Prants (2015) reviewed the applicability of Lagrangian structures computed in backward-time to study several transport problems in the ocean. Comparisons of drifter trajectories with attracting heuristic LCSs computed in backward-time are here carried out with the same aim.

Evaluation of the most influential heuristic LCSs in FTLE fields, i.e. ridges, is pursued considering the dynamical properties of these features (Mathur et al., 2007; Green et al., 2007). Ridges behave as attractors of trajectories solution of the dynamical system

$$\frac{dx}{ds} = \nabla \sigma_0^{t_0+T}(\mathbf{x}) \tag{8}$$

where s is the arclength along the gradient lines of $\sigma_0^{t_0+T}(\mathbf{x})$ and the right-hand side represents the spatial gradient of FTLE scalar fields. This property is at the base of the extraction algorithm proposed by Mathur et al. (2007) and here adopted.

We start the analysis focusing our attention on three reseeding time-windows of Drifters 6, 29 and 42. The choice for selecting these drifters has been motivated in the previous section. For the sake of clarity, the same color coding will be adopted in all figures of this section, namely observed drifters position will be colored in green, simulated drifters without reseeding in red and simulated drifters with reseeding in blue.

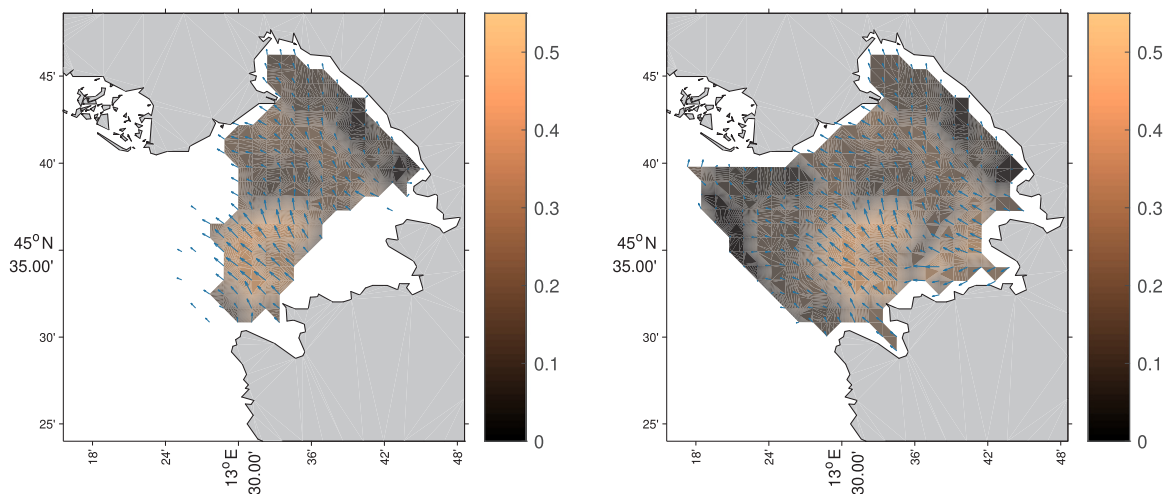


Fig. 4. Example of extrapolation velocity field for 27th April 2012 at 03:00 UTC. Velocity expressed in [m/s]. Right: original measurements. Left: reconstructed velocity field.

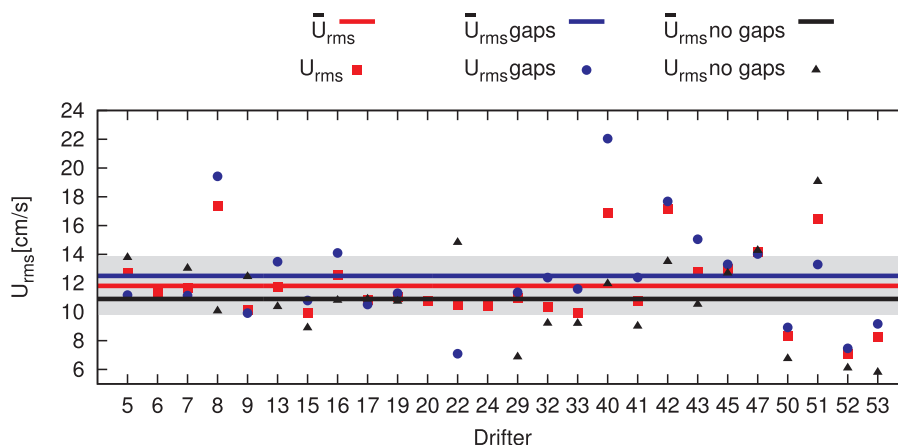


Fig. 5. U_{rms} evaluated for the three cases described in the text: the results obtained with entire dataset in red, results obtained considering the data gaps in blue and, finally, results excluding the data gaps in black. Shaded region indicates the interval of averaged rms plus/minus a standard deviation for the case of the whole dataset. (For interpretation of the references to color in this figure legend, the reader is referred to the web version of this article.)

Then, we will compare the prediction of the drifters position that can be performed using both the heuristic LCSs and a more traditional approach based on the simple computation of a single trajectory, which should represent the path of the drifter. At the end of this section, an overall comparison among the above predictions will be presented for

the entire data sets.

Fig. 8 shows four snapshots of the trajectory of Drifter 6 superimposed to FTLE backward fields (attracting heuristic LCSs). Panel a) refers to the second time-step of the reseeding time-window and shows that the simulated drifter without reseeding has already headed

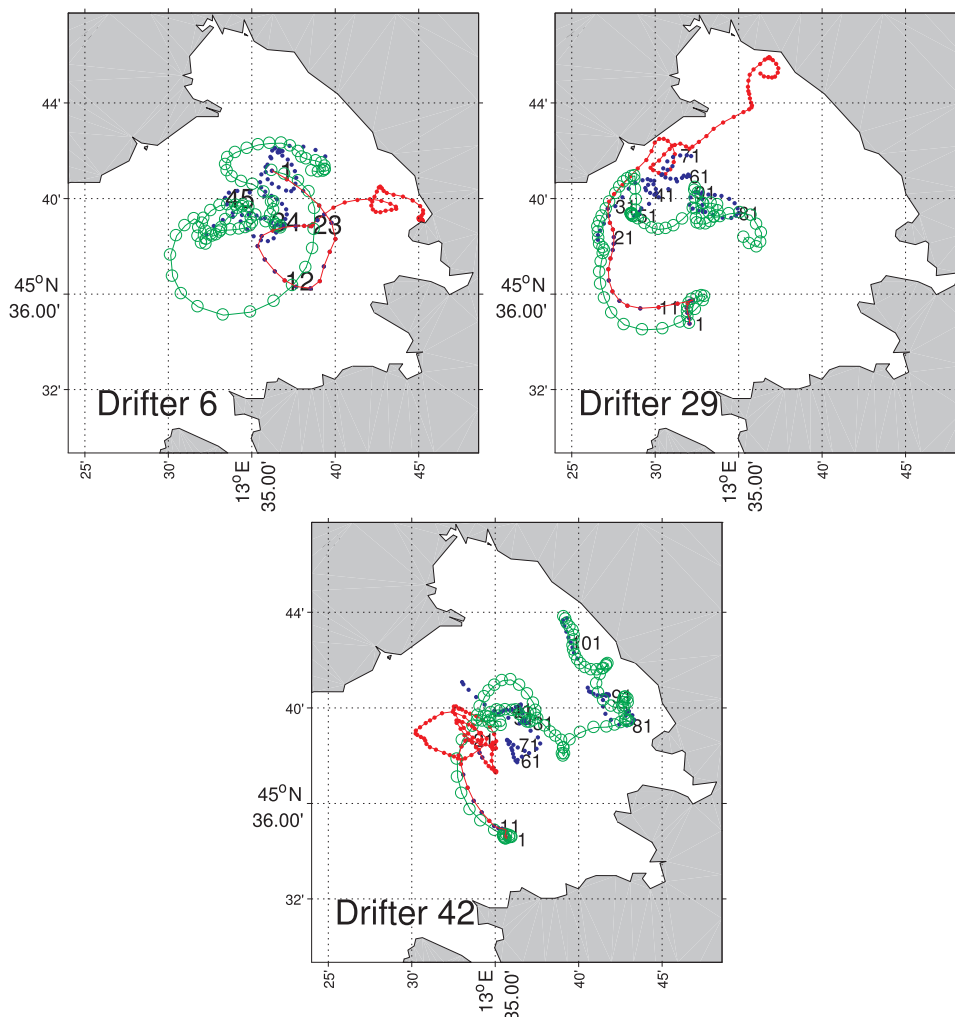


Fig. 6. Examples of trajectories of real drifters in green, simulated in red and reseeded in blue. The numbers on each map show the evolution in time (hours) of the reseeded drifter (blue). (For interpretation of the references to color in this figure legend, the reader is referred to the web version of this article.)

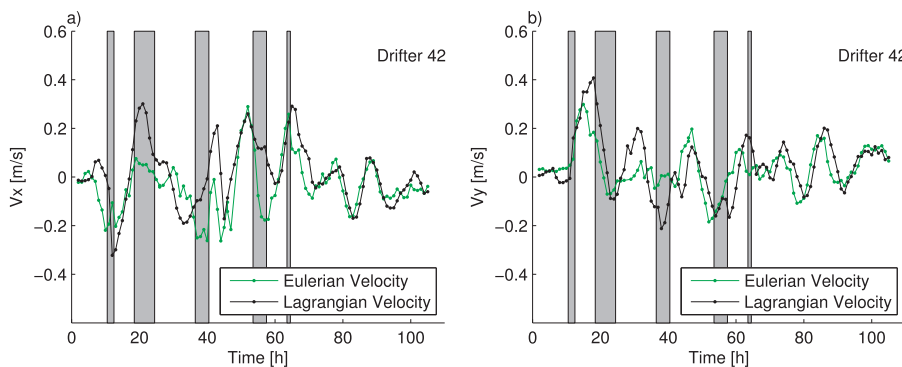


Fig. 7. Comparison of Eulerian and Lagrangian velocities of drifter 42. Shaded areas show data gaps.

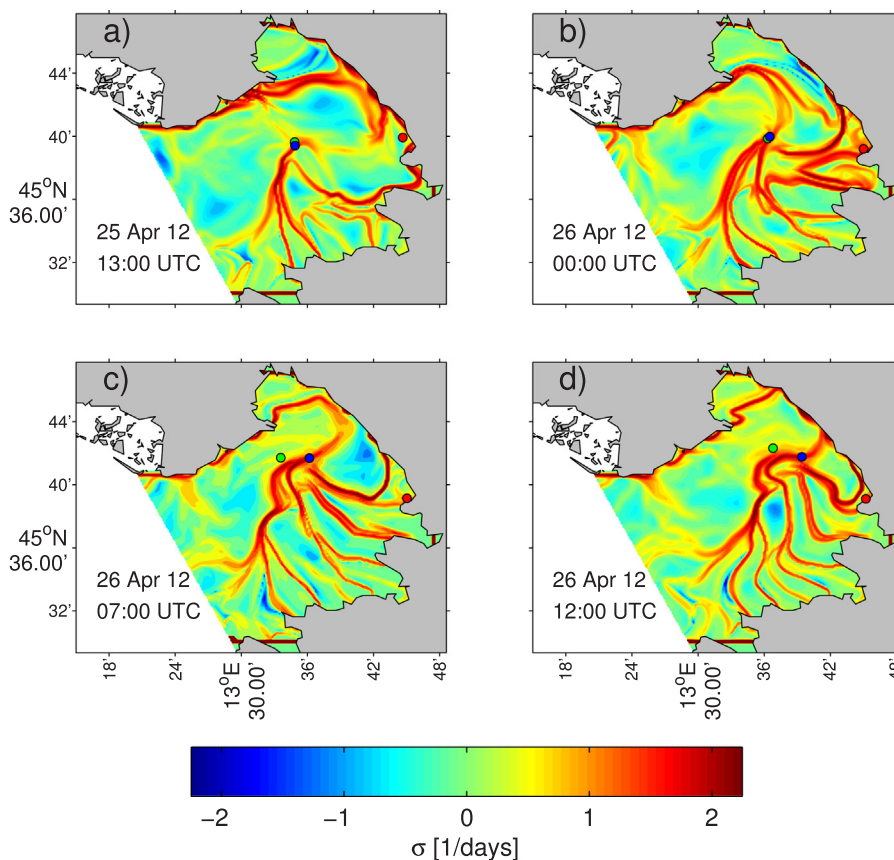


Fig. 8. Drifter 6 and backward FTLE fields (attracting structures) for 25th April 2012 13:00 UTC, Panel a), 26th April 2012 00:00, 07:00 and 12:00 UTC, Panel b), c) and d), respectively. Green drifter: field surveyed during TOSCA campaign; red drifter: numerical simulated without reseeding; blue drifter: numerical simulated with reseeding every 24 h. These four panels attain the second reseeding time-window. As a result, the red drifter has already separated from the green one. (For interpretation of the references to color in this figure legend, the reader is referred to the web version of this article.)

towards the eastern part of the GoT, see red dot, separating from the real drifter. On the contrary, the observed and the simulated trajectories with reseeding are tied to the structures present at the center of the GoT in all four Panels.

Moving to the analysis of Drifter 29, see Fig. 9, it is interesting to note that the deployment of the drifter occurs in a position initially quite distant from any relevant attracting heuristic LCSs, see Fig. 9 panel a). However, as time elapses the drifter tends to move towards the closest attracting structure. Moreover, even in this case, the simulated drifter without reseeding significantly separates from the observed one. However, the reseeded drifter and the simulated one show different dynamics. The real one tends to move towards the center of the GoT, whereas the reseeded drifter is confined in the north-western part of the GoT. In order to understand the reasons behind this difference, we

analyze also the forward FTLE fields, i.e. repelling structures. Panels a) to d) of Fig. 10 are the corresponding forward FTLE fields of the backward FTLE fields of panels a) to d) of Fig. 9. Panel a) of Fig. 10 shows that observed and reseeded drifters are in the proximity of a repelling structure at the beginning of the reseeding time-window. In the following time steps a small separation between the two trajectories will result afterwards in greater separation: observed and simulated drifters are divided by such structure during the whole time-window under consideration. This justifies the greater separation observed for Drifter 29 compared to Drifter 6. It is also possible to argue that sensitivity to initial conditions and unresolved subgrid dynamics play a role that is not modelled integrating Eq. (1) on the base of the velocity fields at our disposal.

Considering Drifter 42, Fig. 11 shows the superposition of

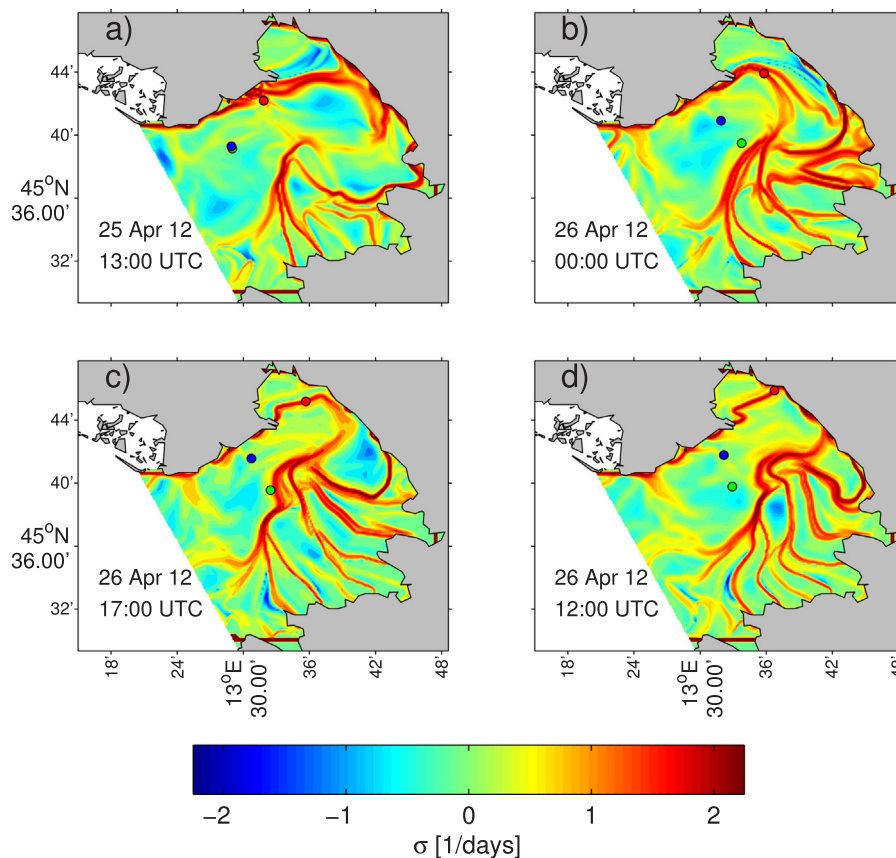


Fig. 9. Drifter 29 and backward FTLE (attracting structures) fields for 25th April 2012 13:00 UTC, Panel a), 26th April 2012 00:00, 07:00 and 12:00 UTC, Panel b), c) and d), respectively. Green drifter: field surveyed during TOSCA campaign; red drifter: numerical simulated without reseeding; blue drifter: numerical simulated with reseeding every 24 h. These four panels attain the second reseeding time-window. As a result, the red drifter has already separated from the green one. (For interpretation of the references to color in this figure legend, the reader is referred to the web version of this article.)

trajectories of Drifter 42 on backward-time FTLE fields, i.e. attracting structures. The results reveal that the observed drifter and the simulated ones move along local maxima of FTLE fields and head to the opposite sides of the GoT (the real drifter heads towards west, the simulated one heads toward the eastern side and the reseeded simulated stays at the center of the GoT). Such local maxima belong to ridges of FTLE fields detected in agreement with Mathur et al. (2007).

Fig. 12 shows such ridges detected on the FTLE field of Panel a) of Fig. 11. In particular, the simulated drifter without reseeding is bound to a structure identified as ST1, while the observed and the reseeded simulated are attracted by a structure identified as ST2. The structure ST2 develops from a prevailing north-west to south-east direction to a prevailing east to west direction. Analogously to the case of Drifter 29, subgrid dynamics influences the path of the drifter and FTLEs prove to be able to capture direction along which transport develops.

We now compute two types of distances. Firstly, between the observed position of the drifter and the numerical trajectories and, secondly, between the observed position of the drifter and the attracting heuristic LCSs for a time interval of 24 h for the three drifters discussed above. The resulting distances are reported in Fig. 13. The ridges taken into account are those at the center of the GoT for Drifter 6 and 29, whereas for Drifter 42 the ridge ST2 is considered. The separation between observed and reseeded drifters tends to increase in time from zero to several kilometers (dotted lines in Fig. 13). On the contrary, the initial separation between attracting structures and drifters can be significant at the beginning of the time-window and decreases as the trajectory evolves, owing to the attracting nature of the LCSs, see for instance Drifter 29. In all these three cases analyzed, at the end of the time-window, separations between observations and simulated drifters is greater than distances between drifters and ridges (below 2.5 km).

Repeating this procedure with the entire drifters data sets, we finally obtain the results shown in Fig. 14, where the same quantities have been calculated for each drifter for the same 24 h time frame. On average, the distance of real drifters from the nearest FTLE-backward-ridge is 1.42 ± 1.05 km whilst the separation between observations and reseeded simulated drifters is on average 7.80 ± 2.87 km, thus, more than five times larger.

It could be useful to illustrate the consequences of the above considerations through an ideal example. Imagine to carry out a SaR operation in the sea having at your disposal the position where the accident occurred and velocity fields provided by measurements or validated numerical models. Detection of Lagrangian structures could contribute to the established methods based on trajectory computations (Jordi et al., 2006; Breivik and Allen, 2008). Lagrangian structures could highlight preferred directions along which search operations should be carried out. Several Authors, see among others Ullman et al. (2006); Molcard et al. (2009) and Bellomo et al. (2015), suggest the use of single particle trajectories, based on radar velocities, as the simplest predictive strategy for operational application such as SaR. We intend to compare the accuracy of the above method against the employment of the LCSs instead of the single particle computation. Indeed, Molcard et al. (2009) carried out an extensive comparison between real drifters trajectories and reseeded drifters and their applicability for operational purposes. In order to quantify the reliability of drifter trajectory predictions, they evaluated the mean separation distance $d(t)$ and the mean displacement $D(t)$. They associated $D(t)$ to the prediction error assuming the drifter stays where it is deployed, which is the case where no information is available (“no information strategy”), while $d(t)$ indicates the error of the prediction based on the radar velocity field. The ratio d/D or its inverse defined in Bellomo et al. (2015) as search range

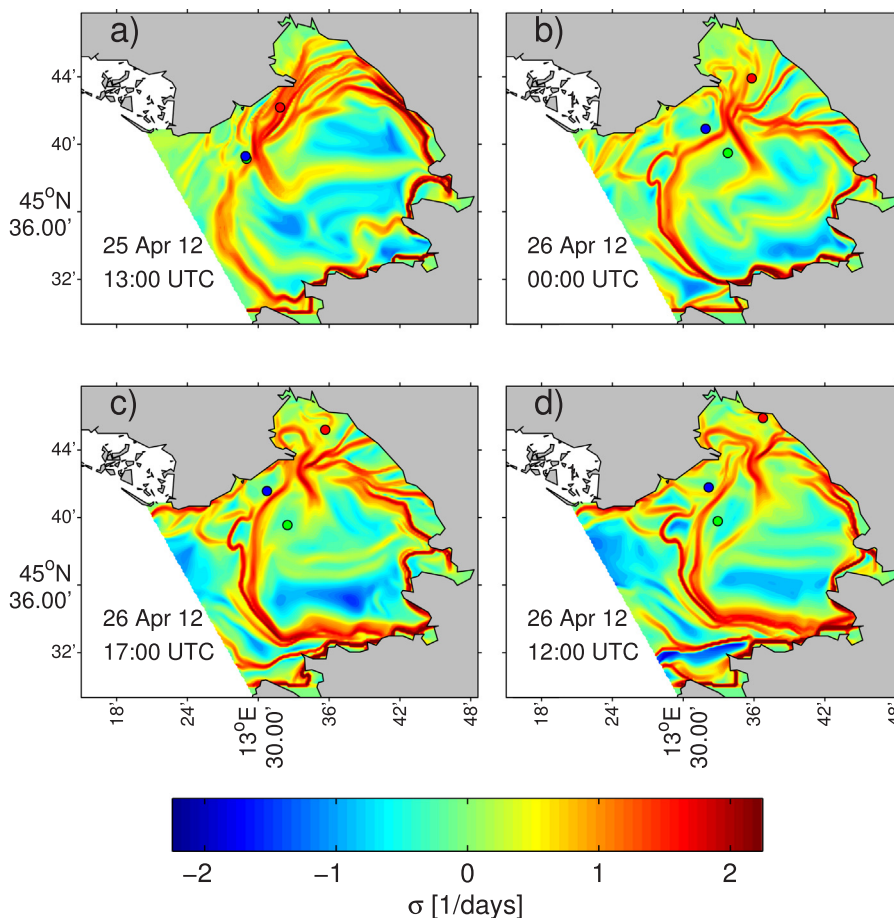


Fig. 10. Drifter 29 and forward FTLE fields (repelling structures) for 25th April 2012 13:00 UTC, Panel a), and 26th April 2012 00:00 UTC, Panel b). Green drifter: field surveyed during TOSCA campaign; red drifter: numerical simulated without reseeding; blue drifter: numerical simulated with reseeding every 24 h. (For interpretation of the references to color in this figure legend, the reader is referred to the web version of this article.).

reduction factor (SRRF), provides an estimate of the reduction of the error committed in the “no information strategy” due to the radar measurements. Estimates of the above ratio for integration intervals of 24 h are presented in Ullman et al. (2006) and Molcard et al. (2009) and the resulting values are of the order of 1/2 or greater. Moreover, Bellomo et al. (2015) evaluated these quantity for different sites interested by the TOSCA project obtaining a ratio always smaller than the unity over time windows of 12 or 24 h. In particular, for the Gulf of Trieste, they computed the SRRF for a time interval of 12 h obtaining a value of about 1.6, which implies a value of the ratio d/D close to 0.6. Moving to the results obtained from the analysis of the LCSs and their distance to the observed drifters positions, see Fig. 14, it is possible to compute the ratio $d(t)/D(t)$ or its inverse, i.e. the SRRF factor, substituting the distance $d(t)$ obtained from single particle trajectories with the distance to the heuristic LCSs after a time interval of 24 h. The values obtained for $d(t)/D(t)$ ranges from a minimum of 0.03 to a maximum of 0.51 with an averaged value of 0.17. The corresponding values of the SRRF factor as defined by Bellomo et al. (2015) are 1.96, 36 and 10.5, respectively. The value computed by Bellomo et al. (2015) and reported in the paper is much less and, furthermore, evaluated on a time interval of 12 h. Note also that in several cases, the employment of the single particle strategy leads to values of the ratio $d(t)/D(t)$ bigger than unity, implying that this prediction is not helpful during a SaR operation, while in the case of heuristic LCSs for all tested drifters we obtain values much smaller than one.

Finally, the results suggest that these two approaches should be carried out jointly in order to better assess the approximated position of the target of SaR operations. Fig. 15 represents a simple sketch of the

searching strategy that is possible to adopt. By locating repelling and attracting structures, it is possible to focus SaR operations along a narrow strip surrounding the attracting heuristic LCS. However, in order to define how elongated this area should be it is possible to join the heuristic LCS analysis to the single-particle tracking procedure. If a single-particle predictive strategy is carried out, the search for the passive object should extend on circles whose maximum radius has an order of magnitude of the average distance plus the standard deviation. By joining these two approaches, the area where the SaR operations are to be carried out is the shaded area represented at the bottom of Fig. 15 consisting in the superposition of the elongated strip around the heuristic LCS and the circle. In the next Section we will apply this idea considering LCS evaluated from Cauchy-Green tensorlines.

6. Detection of lagrangian coherent structures

Motivated by the good agreement between drifters and heuristic LCSs reported in the previous Section, we carry out an analysis based on rigorous LCSs. We adopt the same procedure described by Olascoaga et al. (2013). We locate tensorlines of the Cauchy-Green tensor, i.e. curves tangent to its eigenvectors. Let ξ_1 and ξ_2 be the eigenvectors of the Cauchy-Green tensor associated with the minimum and maximum eigenvalues ($0 < \lambda_1 \leq \lambda_2$), respectively, and $\xi_1 \perp \xi_2$. The Cauchy-Green tensor is evaluated on the fixed time interval $[t_0, t_0 + T]$ with a forward integration. Shrinklines at time t_0 are identified as trajectories of

$$\mathbf{r}' = \xi_1 \tag{9}$$

Stretchlines at time t_0 are identified as trajectories of

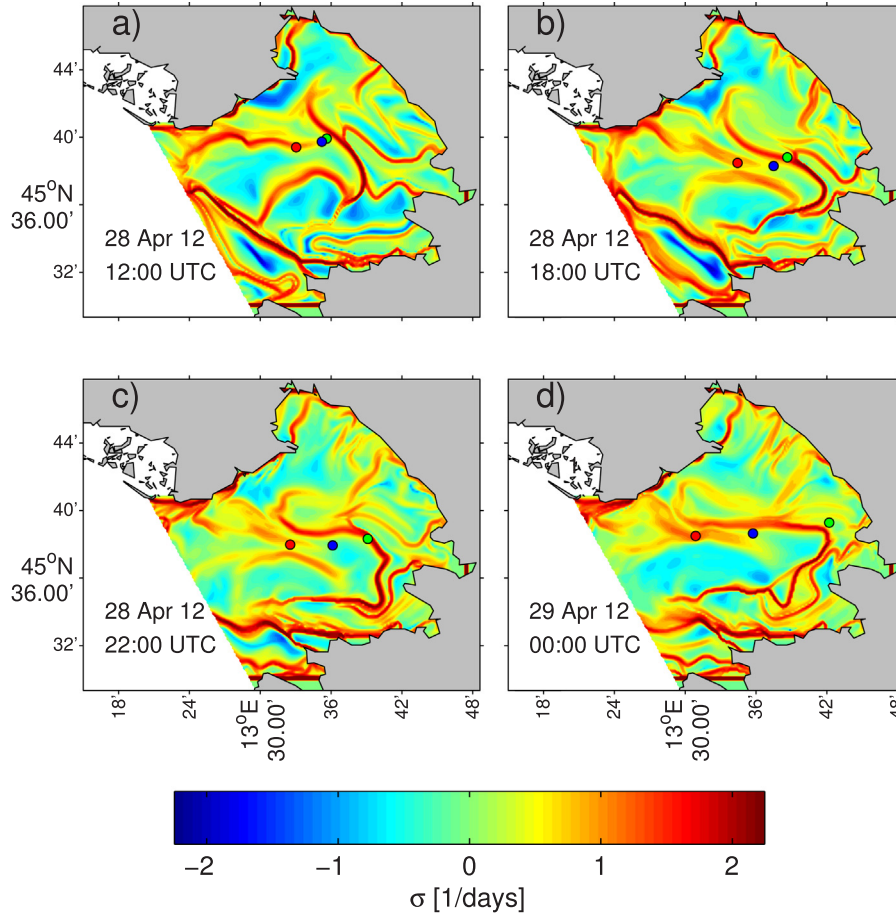


Fig. 11. Drifter 42 and backward FTLE fields (attracting structures) for 28th April 2012 12:00, 18:00 and 22:00 UTC, Panel a), b) and c), 29th April 2012 00:00, 03:00 and 05:00 UTC, Panel d), e) and f), respectively. Green drifter: field surveyed during TOSCA campaign; red drifter: numerical simulated without reseeding; blue drifter: numerical simulated with reseeding every 24 h. (For interpretation of the references to color in this figure legend, the reader is referred to the web version of this article.)

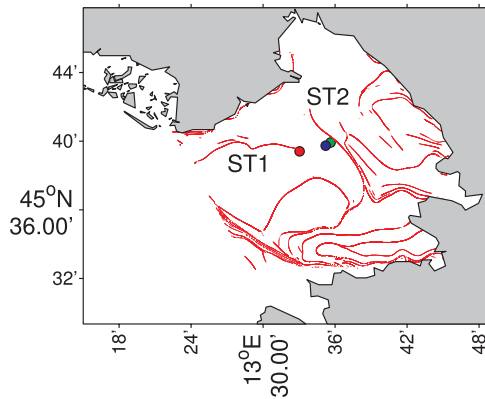


Fig. 12. Drifter 42 and backward FTLE ridges (attracting structures) for 28th April 2012 12:00 UTC. Green drifter: field surveyed during TOSCA campaign; red drifter: numerical simulated without reseeding; blue drifter: numerical simulated with reseeding every 24 h. (For interpretation of the references to color in this figure legend, the reader is referred to the web version of this article.)

$$\mathbf{r}' = \xi_2 \quad (10)$$

In order to locate the most repelling and attracting LCSs at the time t_0 we retain the ones that exhibit the highest repulsion and attraction, respectively. The normal growth to a material line of a unit normal vector is given by the repulsion rate $\rho_{t_0}^{t_0+T}$ (Haller, 2011). Squeezelines and stretchlines present a repulsion rate $\rho_{t_0}^{t_0+T} = \sqrt{\lambda_2(x)}$ and

$\rho_{t_0}^{t_0+T} = \sqrt{\lambda_1(x)}$, respectively. The most prominent attracting and repelling LCSs are chosen as those that on average show the maximum repulsion and attraction along their length. Let the curve γ be a LCS, the average is computed as (Haller and Beron-Vera, 2012; Farazmand and Haller, 2013)

$$\langle \rho_{t_0}^{t_0+T} \rangle = \frac{\int_{\gamma} \rho_{t_0}^{t_0+T} |r'(s)| ds}{\int_{\gamma} |r'(s)| ds} \quad (11)$$

In order to locate attracting LCSs at any time $t \in [t_0, t_0 + T]$ we advect in forward time the LCSs detected at time t_0 .

Comparison of LCSs with Drifter 42 is illuminating. We seek in the neighbour of the deployment location of Drifter 42 the most repelling and attracting LCSs and we advect the latter in forward time. We repeat the procedure for every reseeding time-window. Besides, we apply the operational procedure depicted in Fig. 15. These results are plotted in Fig. 16 (cf. with Fig. 11) where four snapshots of the evolution of the drifter trajectories (observed and simulated) alongside with LCSs are shown. In particular, a circle of radius 7.52 km (the average distance between observed and reseeded drifter after 24 h, cf. Fig. 14) is centred at the reseeded drifter position and represents the searching area due to a single-particle approach. Panel a) of Fig. 16 shows blue and black curves representing attracting and repelling LCSs, respectively. The black point represent the intersection between LCSs, i.e. a hyperbolic point. The black dashed curves represent the searching areas alongside the attracting LCSs in analogy to Fig. 15. The scalar field underneath is the backward FTLE field. Ridges of this field are proxies of attracting LCSs and a quite good agreement is shown especially in panel d). It is

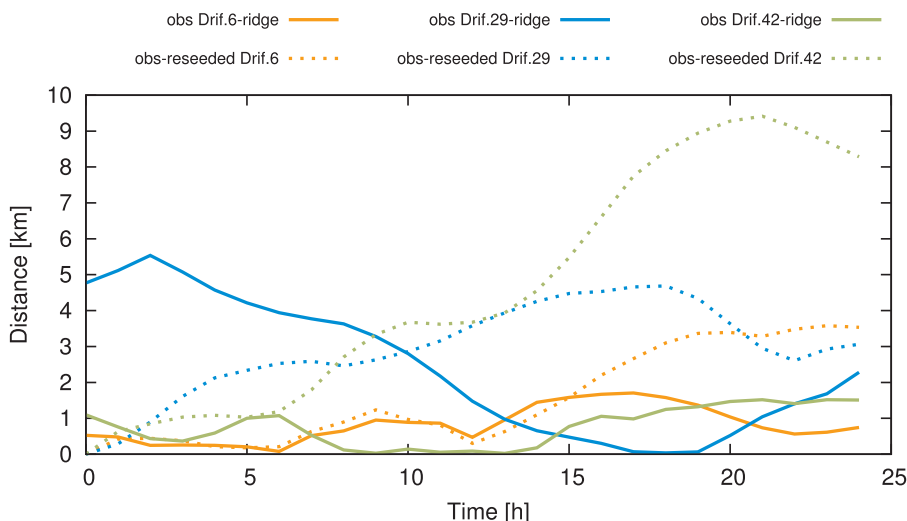


Fig. 13. Distances of real and reseeded drifters from backward FTLE ridges and between themselves.

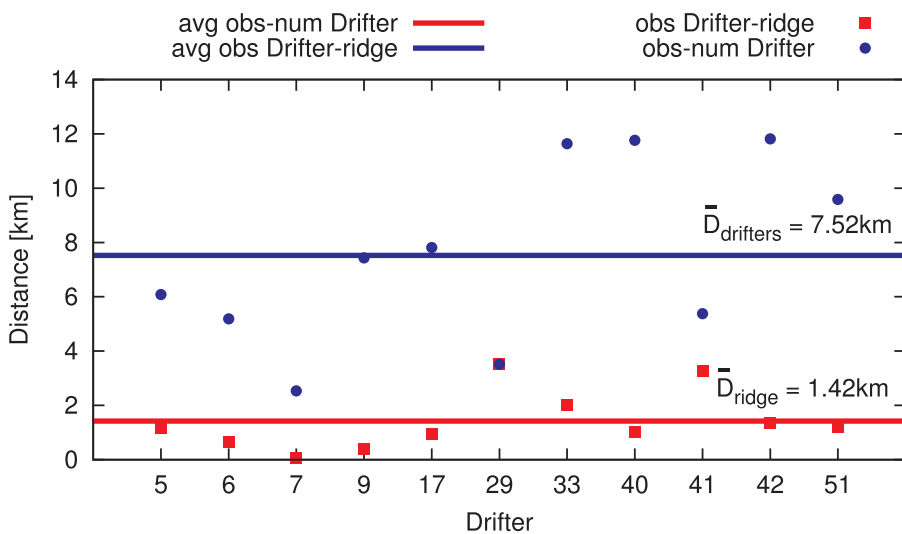


Fig. 14. Summary of the computed differences between the simulated drifters and the corresponding observed position (blue dots), the differences between the observed drifters positions and the attracting LCSs (red dots) and, finally, the corresponding averaged values. Separations are computed using the positions obtained after 24 h simulations. (For interpretation of the references to color in this figure legend, the reader is referred to the web version of this article.).

evident that the searching area is greatly reduced by adopting such a combined approach. Since the dashed curves and the dark circle represent averaged values, the observed drifter (depicted in green) can take a position outside of such a region. This occurs in panel d) of Fig. 16. Since shrinklines represent unstable lines they cannot be advected in forward time. Therefore, panels b), c) and d) show only attracting LCS. Notably, the evolution of the attracting LCS follows the same pattern of attracting heuristic LCSs depicted in Fig. 11 leading to a prevailing east to west elongation.

7. Conclusions

In the present work we investigate transport phenomena in the Gulf of Trieste by analyzing velocity fields measured by the network of coastal HF-radars of the TOSCA project.

In the framework of the TOSCA campaign drifters were deployed in the sea and therefore the reliability of our results is assessed via analysis based on real trajectories. Transport can be studied through the concurrent use of finite-time and finite-size Lyapunov exponents (FTLEs and FSLEs) and Lagrangian Coherent Structures (LCSs). A direct comparison of FTLEs and FSLEs by evaluating their correlation is carried out showing the agreement between them. To our knowledge only Boffetta et al. (2001) and Peikert et al. (2014) carried out a direct comparison between FTLEs and FSLEs. However, their analyses were

only based on numerical cases. The present results show that both FTLEs and FSLEs fields are able to locate in real geophysical flows characterized by large Reynolds numbers the same pattern of Lagrangian structures, as commonly defined in literature. Indeed, the idea introduced by Peikert et al. (2014) that with an adequate choice of the main controlling parameters for FTLE and FSLE identification, i.e. the integration time T and the final separation δ_f , the two measures lead to comparable results is herein confirmed and strengthened.

Moreover, the analyses based on Lyapunov-exponent scalar fields is beneficial with respect to ones based uniquely on the drifter-tracking. Lyapunov-exponents prove to be a valuable tool in order to evaluate the main directions along which transport phenomena are likely to occur. Despite Lyapunov-exponent diagnostics have not been employed yet as a forecasting method, this analysis shows the usefulness in nowcasting applications (Lekien et al., 2005; Shadden et al., 2009; Tang et al., 2011; Peacock and Haller, 2013), i.e. the accurate description of the present state of a system. It is possible to imagine that thanks to a real-time data acquisition system of velocity fields, the possible directions passive tracers could spread towards are highlighted by means of Lagrangian structures detected in real time. Therefore, if inaccurate velocity information and subgrid dynamics could decrease the reliability of single-particle tracking of passive tracers, an analysis carried out jointly with Lyapunov-exponents could shed some light on such uncertainties and give significant insight about the preferred direction of

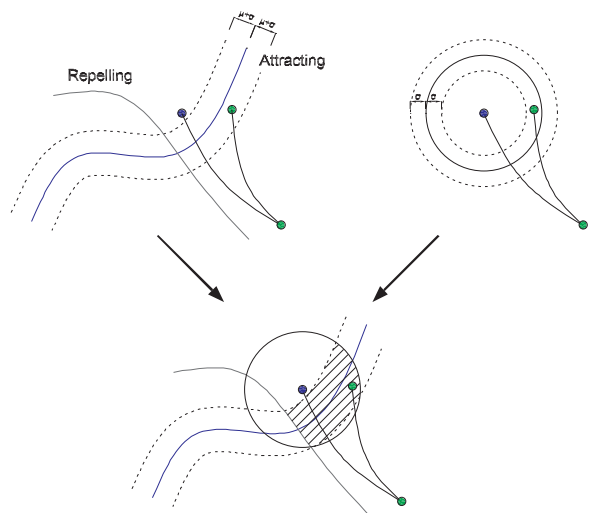


Fig. 15. Sketch of LCSs and observed drifter mutual positions, on the left, and of single-particle simulation, on the right. μ represents the average distance while σ the standard deviation. If a single-particle simulation is carried out, the observed drifter and the reseeded drifter tend to have divergent trajectories as time elapses. Therefore, a search operation based on such a simulation should be carried on concentric circles centred on the reseeded drifter, while LCSs give preferential direction along which the search operation can be carried out. Joining these two approaches leads to the evaluation of the area over which SaR operations should be carried out. This area (shaded in the sketch) is the result of the superposition of the circle and of the surrounding strip around attracting LCSs.

occurring transport phenomena. Heuristic LCSs have proven to be more robust against possible inaccuracy of the starting velocity fields than more standard Lagrangian approaches based on single numerical trajectories. The averaged difference between drifters and LCSs is estimated to be of the order of 1.5 km instead of about 7 km of the trajectory approach. Besides, LCSs computed following [Olascoaga et al. \(2013\)](#) could be directly applied in nowcasting application. However, it must be kept in mind that the better result obtained with LCSs is inherent with their elongated nature compared to the trajectory approach based on a point-to-point distances.

At the end of their seminal work [Molcard et al. \(2009\)](#) wondered “whether or not dynamical system methods such as FSLE and FTLE can be applied to small coastal areas”. The present work answers positively the question and goes beyond by computing LCSs as most attracting and repelling Cauchy-Green tensorlines in a Mediterranean coastal environment. The development of nowcasting application, for instance directed to SaR operations, should rely on the joint use of LCSs and single-particle tracking as suggested in the present work.

Acknowledgements

The present research has been funded by Progetto di Ricerca di Ateneo 2010, Università degli Studi di Genova. Francesco Enrile has been founded by PADI Foundation grant 2015. The authors gratefully acknowledge support from the MED TOSCA project, co-financed by the European Regional Development Fund. Support from the Italian Flagship Project RITMARE is also acknowledged.

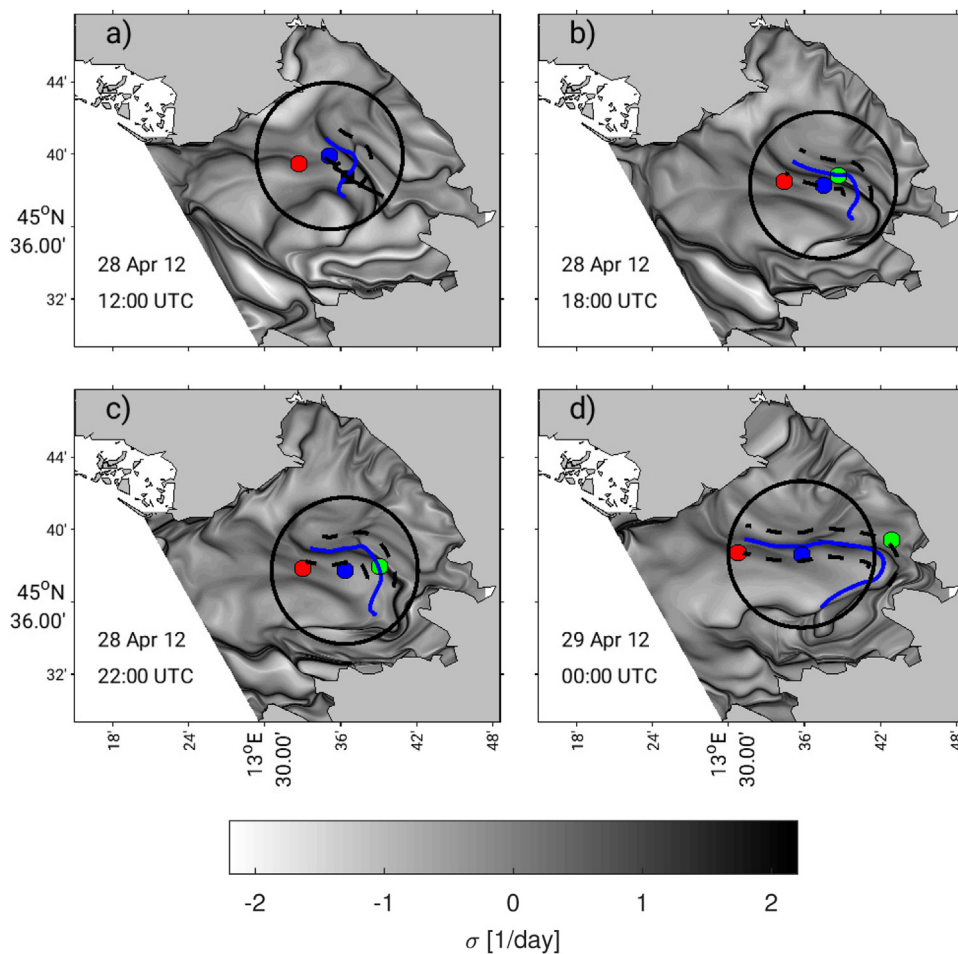


Fig. 16. Application of the conceptual sketch of [Fig. 15](#). Attracting LCS in blue and repelling LCS in black. The black dot is the intersection between attracting and repelling LCS. Green, blue and red dots are observed and simulated drifters with and without reseeding, respectively. The scalar field underneath is the backward FTLE field. The black circle represents the searching area due to a single-particle tracking. The dashed curves are the searching areas alongside the attracting LCS. By combining these two approaches a better prediction can be obtained. The four panels represent the same time instances of [Fig. 11](#). Average values are adopted in order to plot circles and dashed curves. (For interpretation of the references to color in this figure legend, the reader is referred to the web version of this article.)

References

- Abraham, E.R., Bowen, M.M., 2002. Chaotic stirring by a mesoscale surface ocean-flow. *Chaos* 12 (2), 373–381.
- Allshouse, M.R., Peacock, T., 2015a. Lagrangian based methods for coherent structures detection. *Chaos* 25, 9.
- Allshouse, M.R., Peacock, T., 2015b. Refining finite-time Lyapunov exponent ridges and the challenges of classifying them. *Chaos* 25, 8.
- Alvera-Azcárate, A., Barth, A., Sirjacobs, D., Beckers, J., 2009. Enhancing temporal correlations in EOF expansions for the reconstruction of missing data using DINEOF. *Ocean Sci.* 5, 5–11.
- Alvera-Azcárate, A., Barth, A., Sirjacobs, D., Lenartz, F., Beckers, J., 2011. Data interpolating empirical orthogonal functions (DINEOF): a tool for geophysical data analysis. *Mediterr. Mar. Sci.* 12.
- Barrick, D.E., Lipa, B., 1986. An evaluation of least-squares and closed-form dual-angle methods for CODAR surface-current applications. *IEEE J. Ocean. Eng.* 11, 322–326.
- Bellomo, L., Griffa, A., Cosoli, S., Falco, P., Gerin, R., Iermano, I., Kalampokis, A., Kokkini, Z., Lana, A., Magaldi, M., Mamoutos, I., Mantovani, C., Marmain, J., Potiris, E., Sayol, J., Barbin, Y., Berta, M., Borghini, M., Bussani, A., Corgnati, L., Dagneaux, Q., Gaggelli, J., Guterman, P., Mallarino, D., Mazzoldi, A., Molcard, A., Orfila, A., Poulain, P.-M., Quentin, C., Tintoré, J., Uttieri, M., Vetrano, A., Zambianchi, E., Zervakis, V., 2015. Toward an integrated HF radar network in the Mediterranean Sea to improve search and rescue and oil spill response: the TOSCA project experience. *J. Oper. Oceanogr.* 8 (2), 95–107.
- Berta, M., Bellomo, L., Magaldi, M.G., Griffa, A., Molcard, A., Marmain, J., Borghini, M., Taillandier, V., 2014a. Estimating Lagrangian transport blending drifters with HF radar data and models: results from the TOSCA experiment in the Ligurian Current (North Western Mediterranean Sea). *Prog. Oceanogr.* 128 (Supplement C), S15–S29.
- Berta, M., Ursella, L., Nencioli, F., Doglioli, A., Petrenko, A., Cosoli, S., 2014b. Surface transport in the Northeastern Adriatic Sea from FSLE analysis of HF-Radar measurements. *Cont. Shelf Res.* 77, 14–23.
- Boffetta, G., Lacorata, G., Redaelli, G., Vulpiani, A., 2001. Detecting barriers to transport: a review of different techniques. *Physica D* 159, 58–70.
- Breivik, Ø., Allen, A.A., 2008. An operational search and rescue model for the Norwegian Sea and the North sea. *J. Mar. Syst.* 69 (1–2), 99–113.
- Cencini, M., Vulpiani, A., 2013. Finite size Lyapunov exponent: review on applications. *J. Phys. A: Math. Theor.* 46 (25), 254019.
- Chapman, R.D., Shay, L.K., Graber, H.C., Edson, J.B., Karachintsev, A., Trump, C.L., Ross, D.B., 1997. On the accuracy of HF radar surface current measurements: inter-comparisons with ship-based sensors. *J. Geophys. Res.: Oceans* 102 (C8), 18737–18748.
- Cosoli, S., Ličer, M., Vodopivec, M., Malačič, V., 2013. Surface circulation in the Gulf of Trieste (northern Adriatic Sea) from radar, model, and ADCP comparisons. *J. Geophys. Res.: Oceans* 118 (11), 6183–6200.
- Crombie, D., 1955. Doppler spectrum of sea echo at 13.56 mc/s. *Nature* 175, 681–682.
- Davis, R., 1985. Drifter observations of coastal surface currents during CODE: the method and descriptive view. *J. Geophys. Res.* 90, 4741–4755.
- Farazmand, M., Haller, G., 2013. Attracting and repelling lagrangian coherent structures from a single computation. *Chaos: an Interdisciplinary. J. Nonlinear Sci.* 23 (2), 023101.
- Fischer, H., List, E., Koh, R., Imberger, J., Brooks, N., 1979. *Mixing in Inland and Coastal Waters*. Academic Press.
- Garaboa-Paz, D., Eiras-Barca, J., Huhn, F., Pérez-Muñuzuri, V., 2015. Lagrangian coherent structures along atmospheric rivers. *Chaos* 25, 6.
- Green, M.A., Rowley, C.W., Haller, G., 2007. Detection of lagrangian coherent structures in three-dimensional turbulence. *J. Fluid Mech.* 572 (–1), 111–120.
- Gurgel, K.-W., Antonischki, G., Essen, H.-H., Schlick, T., 1999. Wellen Radar (WERA): a new ground-wave HF-radar for ocean remote sensing. *Coast. Eng.* 37 (3), 219–234.
- Haller, G., 2002. Lagrangian coherent structures from approximate velocity data. *Phys. Fluids* 14, 1851–1861.
- Haller, G., 2011. A variational theory of hyperbolic Lagrangian Coherent Structures. *Physica D* 240, 574–598.
- Haller, G., Beron-Vera, F.J., 2012. Geodesic theory of transport barriers in two-dimensional flows. *Phys. D: Nonlinear Phenom.* 241 (20), 1680–1702.
- Hansen, D., Poulain, P., 1996. Processing of WOCE/TOGA drifter data. *J. Atmos. Ocean Technol.* 13, 900–909.
- Harlan, J., Terrill, E., Hazard, L., Keen, C., Barrick, D., Whelan, C., Howden, S., Kohut, J., 2010. The integrated ocean observing system high-frequency radar network: status and local, regional, and national applications. *Mar. Technol. Soc. J.* 44 (6), 122–132.
- Harrison, C.S., Glatzmaier, G.A., 2012. Lagrangian coherent structures in the California Current System - sensitivities and limitations. *Geophys. Astrophys. Fluid Dyn.* 106 (1), 22–44.
- Haza, A., Griffa, A., Martin, P., Molcard, A., Özgökmen, T., Poje, A., Barbanti, R., Book, J., Poulain, P., Rixen, M., et al., 2007. Model-based directed drifter launches in the Adriatic Sea: results from the DART experiment. *Geophys. Res. Lett.* 34, 10.
- Haza, A.C., Özgökmen, T.M., Griffa, A., Molcard, A., Poulain, P.-M., Peggion, G., 2010. Transport properties in small-scale coastal flows: relative dispersion from VHF radar measurements in the Gulf of La Spezia. *Ocean Dyn.* 60, 861–882.
- Haza, A.C., Poje, A.C., Özgökmen, T.M., Martin, P., 2008. Relative dispersion from a high-resolution coastal model of the Adriatic Sea. *Ocean Model.* 22 (1), 48–65.
- Hernández-Carrasco, I., López, C., Hernández-García, E., Turiel, A., 2011. How reliable are finite-size Lyapunov exponents for the assessment of ocean dynamics? *Ocean Model.* 36 (3), 208–218.
- Hernández-Carrasco, I., Rossi, V., Hernández-García, E., Garçon, V., López, C., 2014. The reduction of plankton biomass induced by mesoscale stirring: a modeling study in the Benguela upwelling. *Deep Sea Res. Part I: Oceanogr. Res. Papers* 83, 65–80.
- Huhn, F., von Kameke, A., Allen-Perkins, S., Montero, P., Venancio, A., Pérez-Muñuzuri, V., 2012. Horizontal lagrangian transport in a tidal-driven estuary. Transport barriers attached to prominent coastal boundaries. *Cont. Shelf Res.* 39–40, 1–13.
- Ivonin, D., Broche, P., Devenon, J., V.I., S., 2004. Validation of HF radar probing of the vertical shear of surface currents by acoustic Doppler current profiler measurements. *Journal of Geophysical Research: Ocean*, p. 109.
- Jordi, A., Ferrer, M.I., Vizoso, G., Orfila, A., Basterretxea, G., Casas, B., Álvarez, A., Roig, D., Garau, B., Martínez, M., Fernández, V., Fornés, A., Ruiz, M., Fornós, J., Balaguer, P., Duarte, C., Rodríguez, I., Alvarez, E., Onken, R., Orfila, P., Tintoré, J., 2006. Scientific management of Mediterranean coastal zone: a hybrid ocean forecasting system for oil spill and search and rescue operations. *Mar. Pollut. Bull.* 53 (5–7), 361–368.
- Karrasch, D., Haller, G., 2013. Do finite-size lyapunov exponents detect coherent structures? *Chaos* 23 (043126), 11.
- LaCasce, J., 2008. Statistics from lagrangian observations. *Prog. Oceanogr.* 77 (1A–29).
- Lekien, F., Coulliette, C., Mariano, A.J., Ryan, E.H., Shay, L.K., Haller, G., Marsden, J., 2005. Pollution release tied to invariant manifolds: a case study for the coast of Florida. *Phys. D: Nonlinear Phenom.* 210 (1–2), 1–20.
- Lipa, B., Barrick, D., 1983. Least-squares methods for the extraction of surface currents from CODAR crossed-loop data: application at ARSLOE. *IEEE J. Ocean. Eng.* 8, 226–253.
- Malačič, V., Petelin, B., 2001. Regional Studies: Gulf of Trieste. In: Cushman-Roisin, B., Gačić, M., Poulain, P.M., Artegiani, A., (Eds.). *Physical Oceanography of the Adriatic Sea. Past, Present and Future*. Kluwer Academic Publishers, Dordrecht, Boston, London, pp. 167–181.
- Malačič, V., Petelin, B., 2009. Climatic circulation in the Gulf of Trieste (Northern Adriatic). *J. Geophys. Res.: Oceans* 114, 1978–2012 (C7).
- Mathur, M., Haller, G., Peacock, T., Ruppert-Felso, J.E., Swinney, H.L., 2007. Uncovering the lagrangian skeleton of turbulence. *Phys. Rev. Lett.* 98 (14), 144502.
- Molcard, A., Poulain, P., Griffa, A., Barbin, Y., Gaggelli, J., De Maistre, J., Rixen, M., 2009. Comparison between VHF radar observations and data from drifter clusters in the gulf of la spezia. *J. Mar. Syst.* 78 (Supplement), S79–S89.
- Ohlmann, C., White, P., Washburn, L., Emery, B., Terrill, E., Otero, M., 2007. Interpretation of coastal HF-radar-derived surface currents with high-resolution drifter data. *J. Atmos. Ocean. Technol.* 24 (4), 666–680.
- Olascoaga, M.J., Beron-Vera, F.J., Haller, G., Triñanes, J., Iskandarani, M., Coelho, E.F., Haus, B.K., Huntley, H.S., Jacobs, G., Kirwan, A.D., Lipphardt, B.L., Özgökmen, T.M., Reniers, H.M., Valle-Levinson, A., A.J., 2013. Drifter motion in the Gulf of Mexico constrained by altimetric Lagrangian coherent structures. *Geophys. Res. Lett.* 40 (23), 6171–6175.
- Paduan, J.D., Rosenfeld, L.K., 1996. Remotely sensed surface currents in Monterey Bay from shore-based HF radar (Coastal Ocean Dynamics Application Radar). *J. Geophys. Res.: Oceans* 101 (C9), 20669–20686.
- Paduan, J.D., Washburn, L., 2013. High-frequency radar observations of ocean surface currents. *Annu. Rev. Mar. Sci.* 5, 115–136.
- Peacock, T., Haller, G., 2013. Lagrangian coherent structures: the hidden skeleton of fluid flows. *Phys. Today* 66, 41–47.
- Peikert, R., Pobitzer, A., Sadlo, F., Schindler, B., 2014. A Comparison of Finite-Time and Finite-Size Lyapunov Exponents Topological Methods in Data Analysis and Visualization III. Springer.
- Peng, J., Dabiri, J.O., 2009. Transport of inertial particles by lagrangian coherent structures: application to predator-prey interaction in jellyfish feeding. *J. Fluid Mech.* 623 (–1), 75–84.
- Poulain, P., 1999. Drifter observations of surface circulation in the Adriatic Sea between December 1994 and March 1996. *J. Mar. Syst.* 20, 231–253.
- Poulain, P., Gerin, R., Mauri, E., Pennel, R., 2009. Wind effects on drogued and undrogued drifters in the Eastern Mediterranean. *J. Atmos. Ocean. Technol.* 26, 1144–1156.
- Prants, S.V., 2015. Backward-in-time methods to simulate large-scale transport and mixing in the ocean. *Phys. Scr.* 90 (7), 074054.
- Rohrs, J., Sperrevik, A.K., Christensen, K.H., Brostrom, G., Breivik, O., 2015. Comparison of hf radar measurements with eulerian and lagrangian surface currents. *Ocean Dyn.* 65, 679–690.
- Sadlo, F., Peikert, R., 2007. Efficient visualization of Lagrangian coherent structures by filtered AMR ridge extraction. *IEEE Trans. Vis. Comput. Graph.* 13 (6), 1456–1463.
- Schmidt, R., 1986. Multiple emitter location and signal parameter estimation. *IEEE Trans. Antennas Propag.* 34, 276–280.
- Shadden, S.C., Lekien, F., Marsden, J.E., 2005. Definition and properties of Lagrangian coherent structures from finite-time Lyapunov exponents in two-dimensional aperiodic flows. *Physica D* 212, 271–304.
- Shadden, S.C., Lekien, F., Paduan, J.D., Chavez, F.P., Marsden, J.E., 2009. The correlation between surface drifters and coherent structures based on high-frequency radar data in Monterey Bay. *Deep Sea Res. Part II: Top. Stud. Oceanogr.* 56 (3–5), 161–172.
- St-Onge-Drouin, S., Winkler, G., Dumais, J.-F., Senneville, S., 2014. Hydrodynamics and spatial separation between two clades of a copepod species complex. *J. Mar. Syst.* 129, 334–342.
- Stewart, R., Joy, J., 1974. HF radio measurements of surface currents. *Deep Sea Res.* 21, 1039–1049.
- Tang, W., Pak Wai, C., Haller, G., 2011. Lagrangian Coherent Structures Analysis of Terminal Winds Detected by Lidar. Part I: turbulence Structures. *J. Appl. Meteorol. Climatol.* 50, 325–338.
- Truesdell, C., Noll, W., 2004. *The Non-Linear Field Theories of Mechanics*. Springer.
- Ullman, D., Donnell, J., Kohut, J., Fake, T., Allen, A., 2006. Trajectory prediction using hf radar surface currents: monte carlo simulations of prediction uncertainties. *J. Geophys. Res.* 111, 475–485.